

Contents lists available at ScienceDirect

## International Journal of Mechanical Sciences

journal homepage: www.elsevier.com/locate/ijmecsci



## Modeling material behavior during continuous bending under tension for inferring the post-necking strain hardening response of ductile sheet metals: Application to DP 780 steel



Timothy J. Barrett, Marko Knezevic\*

Department of Mechanical Engineering, University of New Hampshire, 33 Academic Way, Kingsbury Hall, W119, Durham, NH 03824, United States

#### ARTICLE INFO

# Keywords: Plastic deformation Post-necking strain hardening Continuous bending under tension Finite element method Sheet metal

### ABSTRACT

Continuous bending under tension (CBT) testing can stretch ductile sheet metals significantly more than simple tension (ST) testing. Strength and plastic strain levels increase with the number of CBT cycles and substantially exceed those achieved in ST. Taking advantages of the improved elongation-to-fracture (ETF) achieved by CBT, samples of DP 780 steel are pre-deformed to several strain levels by interrupting their CBT testing. Sub-size specimens are machined from the CBT interrupted specimens and tested in ST. The flow curves from these secondary ST tests are then shifted according to the axial strain accumulated during pre-deformation by CBT to determine a large strain (post-necking) flow curve of the material. The identified large strain flow curve is validated with two approaches. First, the large strain flow curve is used to simulate the load versus displacement curve during CBT to large number of CBT cycles. Second, the curve is used to simulate the flow curves based on the secondary ST testing. The simulations are performed using isotropic hardening (IH) and combined isotropic-kinematic hardening (CIKH) material models. The latter model is calibrated using a set of large strain cyclic tension-compression data. An automated procedure is developed for the creation of sub-size specimens from the finite element (FE) mesh of the interrupted CBT specimen to facilitate efficient secondary ST simulations. The procedure involves cutting of the FE mesh into the sub-size specimen shape by Boolean operations in Abaqus software followed by generation of volume FE mesh and mapping of the state variables. The state variables are mapped to simulate deflection of the specimens, as the residual stress field from the prior CBT simulation evolves to reach a new equilibrium. It is found that the model reproduces the experimental load versus displacement curve, including the succession of spikes and plateaus typical of CBT, very closely. The model also predicts yielding of the interrupted sub-size specimens further verifying the identified curve. The predictions demonstrate the utility of the developed methodology for inferring the post-necking strain hardening behavior of sheets.

#### 1. Introduction

True stress-true strain flow curve of a material must be available to simulate a metal forming process using a macroscopic constitutive law in the finite element method (FEM) [1,2]. The flow response is most commonly measured using simple tension (ST). However, forming operations often strain the material beyond the uniform elongation achieved in ST [3–7]. The ST test allows for characterization of the hardening curve up to the point of necking. The response beyond the point of necking is often approximated using a selected phenomenological hardening laws, which fits the available data before the necking and then extrapolates the post-necking behavior to facilitate the simulations.

To circumvent phenomenological approximations, several more accurate methods have been developed to determine post-necking material behavior. In early works [8], significant experimental efforts were put

\* Corresponding author.

E-mail address: marko.knezevic@unh.edu (M. Knezevic).

into attempting to measure the evolving geometry of the necking profile under ST to analytically correct and compensate for material response. The experimental efforts have been relaxed with the advances of digital image correlation (DIC). The DIC technique enabled accurate measurements of the strain fields in the diffuse neck and studies into the postnecking hardening behavior coupled with FEM modeling of the test [9-13]. The test is iteratively modeled to minimize the difference between calculated and measured strain/displacement fields, while inferring the hardening behavior. However, creating a reliable FEM model capable of dealing with the plastic instability is challenging. As macroscopic constitutive laws within a standard FEM are incapable of predicting location of the diffuse neck in a tensile specimen, artificial notches are introduced. Such discontinuities could create numerical issues. Sometime tapered samples are used to better control the location of the diffuse neck [14]. Selecting appropriate elements and mesh design is essential for simulating the necking profile and underlying large plastic strains. Alternative to FEM, the post-necking hardening behavior of sheets can be accomplished using the virtual fields method (VFM) [15-19], which

is an analytical method minimizing the difference between the external (measured) and internal (calculated) work in the necking zone. The VFM is conceived to circumvent the issues with the FEM mesh and notches but is restricted to thin sheets [20].

Developing a testing methodology capable of measuring postnecking hardening behavior is also challenging. To this end, a tube expansion test has been developed. Here, a tube expands by internal pressure, while simultaneously been exposed to ST. The combination deforms a material to higher strain levels than ST only. The bulge test is another test for post-necking hardening [21,22]. Here, pressure is applied to a circular blank imparting an equibiaxial stress state. Based on the pressure applied, curvature of the bulged specimen, and thickness at the pole, the biaxial stress-strain response is measured. Furthermore, flow curves at high strains could be determined by performing intermittent procedures. Here, the goal is to carefully prepare specimens with a large known pre-strain for the subsequent uniaxial testing. An overview of such procedures is given in [23]. Among these procedure, multi-pass wire-drawing and rolling are particularly suited because of imparting relatively homogeneous compressive deformation [23,24]. More recently a forward rod extrusion process has also been utilized [25]. Finally, a test referred to as the continuous bending under tension (CBT) test has recently been observed to significantly increasing elongation to fracture (ETF) of sheets by suppressing plastic instabilities [26]. For example, over five times improved ETF over ST is observed for DP 1180 steel [27,28]. The CBT test is very similar to ST and is often referred to as a 'stabilized ST test' [29-31]. The only difference is that the specimen is continuously bent/unbent by rollers while pulled in ST. The major difference between ST and CBT is that the gauge section elongates uniformly before necking in ST, while it deforms incrementally in CBT. While periodically in the deformation zone, every material point is subjected to a combination of plastic bending under tension but pure tension outside of the deformation zone. The bending strain amplitude in the deformation zone is approximately constant, while the axial strain is growing during the test. Nevertheless, the strain path during CBT is very similar to ST [32], making it a suitable experiment to study postnecking hardening behavior of materials. Assuming that the strength of a material during CBT pre-straining is independent on the CBT process parameters but solely driven by the achieved strain level, the CBT testing method has been used to infer post necking behavior for several materials [33]. However, the work in [33] has not presented any verification of the identified post-necking curves rationalizing the assumption. Although challenging, the CBT testing can be simulated using FEM [27,34] and, thus, allow for verification of the post necking behavior.

This work is a systematic study into a utility of the interrupted CBT testing method for inferring post-necking hardening behavior using a combination of experiments and modeling. Samples of DP 780 sheet are tested in CBT to variable number of cycles, and then a sub-size tensile specimen is machined out of each pre-deformed CBT sample for secondary ST testing. The flow curves measured by the secondary ST tests are then shifted based on the levels of accumulated strain achieved during the CBT pre-deformation and fit into a large strain flow curve. Considering that the structural effects imparted by the CBT test facilitate stretching of the material beyond the uniform strain in ST, the post-necking behavior is inferred. Subsequently, the identified hardening curve is used as a guess for the FEM simulations of the CBT test along with the von Mises isotropic hardening (IH) model. Moreover, the material parameters pertaining to a combined isotropic-kinematic hardening (CIKH) model are identified using a set of the large strain cyclic data for DP 780. The CIKH model is also ensured to reproduce the identified hardening curve. The CBT load versus displacement curve to large number of CBT cycles and the evolution of yield stress with CBT cycles based on the secondary ST tests are simulated using both IH and CIKH models for verification of the experimentally inferred hardening curve. Following the work on machining distortion [35,36], an automated simulation procedure accounting for distortions due to the evolution of residual stresses while interrupting the CBT testing and per-

Table 1
Chemical composition of DP 780 steel (wt%).

	2	Mn	P	S	Si	Cu	Ni	Cr	Мо
-	).1 Sn				0.014 Ti		0.01 N <sub>2</sub>	0.26	0.332
0	0.003	0.048	0.001	0.003	0.001	0.0001	0.006		

forming the secondary ST tests is developed. Comparisons between the measured and simulated distortions reveal that the trends are captured correctly. Moreover, the good agreement between measured in simulated data in every aspect of the comparisons verifies the assumption i.e. the strength primarily depends on the accumulated strain during pre-deformation, while the cyclic pre-deformation condition effects on the stress state are secondary.

#### 2. Material

Dual-phase (DP) steels belong to a class of advanced high strength steels. These steels have composite microstructures made up of martensite and ferrite. Tradeoffs between strength and ductility of these steels are primarily governed by the volume fraction and distribution of the two phases with their contrasting characteristics [37–41]. The behavior also depends on the grain size and crystal orientation distributions. Local plasticity of DP steels is heterogeneous. For example, regions of large ferrite grains suitably oriented for plastic deformation are soft relative to regions of small ferrite grains [42]. Localizations have been observed within such large ferrite grains. Additionally, ferrite channels between bulky martensite regions and incompatibilities at martensite/ferrite phase interfaces can localize the deformation [38,42,43]. Localizations reduce ETF in sheet metal forming of DP steels [44–49].

DP 780 steel of interest in the present work has been obtained as a 1.4 mm rolled sheet from US Steel. It is from US Steels' hot dip (HD) processing lines supplied as galvannealed (HDGA) coated. Its chemical compositions is given in Table 1.

## 3. CBT testing

In earlier works, we have presented a design of a specialized CBT testing device [50,51]. A photograph identifying the main components of the device and process variables is given in Fig. 1. A moving carriage holds a testing specimen and the axial loading system. The device further features a stationary roller assembly mounted on the machine base and a control and data acquisition hardware and software. The carriage reciprocates during the CBT test with a roller velocity of 66 mm/s. The top roller is vertically adjustable to set a bending depth,  $\delta$ . One donutstyle Futek load cell, LCF 450 (capacity of 22.24 kN) is attached to the carriage and another cell, LTH 500 (capacity of 22.24 kN) is attached to the actuator. The hydraulic actuator supplying pulling (crosshead) velocity has a Balluff Micropulse BTL7-A501-M0305-Z-S32 position sensor with a resolution of 5  $\mu$ m. The carriage motion is limited by a pair of limit switches, one positioned on the grip attached to the hydraulic cylinder and another positioned on the base. Limit switches signal the end of the stroke and reversion for the carriage. More details in terms of the machine design can be found in [51,52].

Fig. 2 shows a CBT specimen geometry with the  $1\times$ ,  $2\times$ , and  $3\times$  deformation regions indicated in the drawing and an ASTM E8 sub-size specimen machined from the CBT specimen for secondary ST testing [53]. The deformation regions are defined based on the number of bending cycles for the specimen during each CBT pass. We adopt the following definitions: a 'pass' is described as the rollers traverse the entire gauge length in one direction from one to the other side of the specimen, while a 'CBT cycle' is described as the rollers traverse the gauge length to the other side and then return back over the gauge section to the initial side.

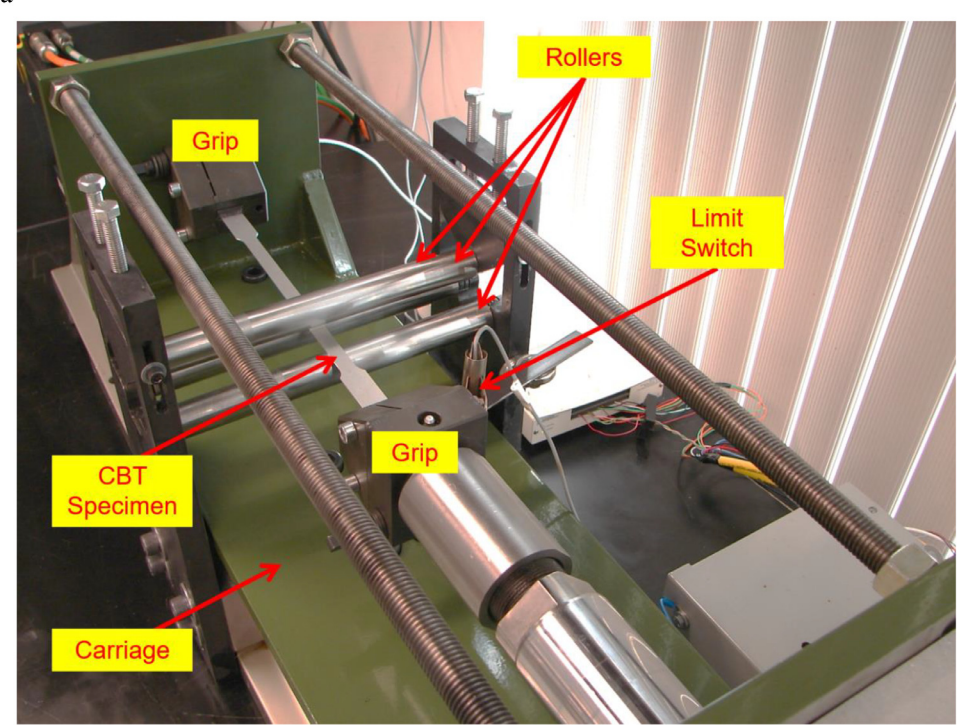
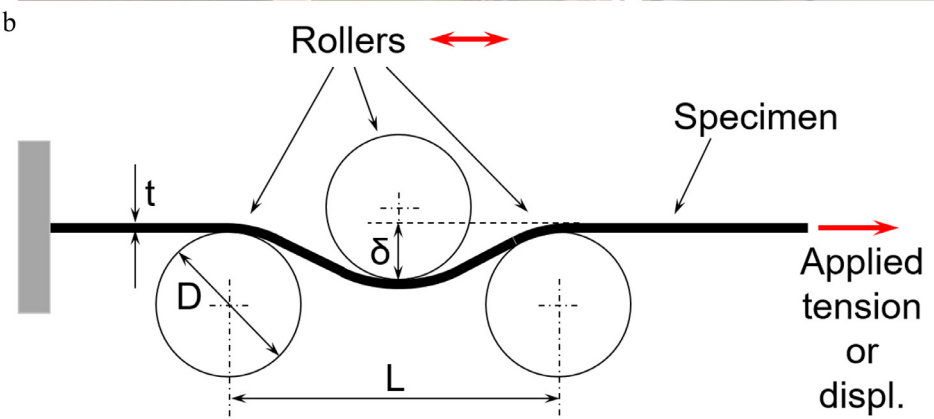


**Fig. 1.** (a) A photo of the CBT testing machine main components. (b) Definition of the main process variables: bending depth,  $\delta$ , set by adjusting the top roller vertically, sheet thickness, t, diameters of rollers, D = 25.4 mm, and distance between the bottom rollers, L = 54 mm.



In the 1x deformation region, the sheet undergoes only one bending and unbending per pass. The 1x deformation region is near the grips. In the 2x deformation region, the sheet is bent and unbent two times. Finally, in the 3x deformation region, the sheet is bent and unbent three times. The 3x region occupies the largest center region of the sample. The gauge section of 200 mm for the CBT specimen is set such that the rollers never exit the gauge section of a standard ASTM E8 ST specimen. The limit switch setup allows every pass to be a bit longer making the 3x deformation region a bit longer, while the 1x and 2x deformation regions have constant respective lengths.

## 4. FEM simulation setups

Fig. 3 shows the simulation setups used to model the CBT test and the secondary ST tests. The simulations were performed using the Abaqus 6.13 implicit FE solver [54–56]. The simulations were created out to match the experiments as closely as possible. The pull rate is calculated using a linear fit of the experimental data as shown in Fig. 3a. The carriage velocity (roller velocity) profile is imported from the experiment, as shown in Fig. 3b. The velocity is about 66 mm/s, after acceleration/deceleration stages. The rollers are free to rotate while they are translated along the length of the speci-

men. The stroke of the rollers covers the sample gauge section, which changes (slightly increases) with every cycle as determined by the limit switches.

The simulation setup for the CBT simulations consists of four objects, three rollers and half of the specimen, since mirror symmetry is imposed along the length of the specimen (Fig. 3c and d). The rollers were modeled as three analytically rigid cylinders of 25.4 mm diameter. Contact is enforced using default state-based tracking, which ensures that nodes on the sample do not penetrate the surface of the rollers. Bending is applied by displacing the center roller to a bending depth of  $\delta = 2.6$  mm. Friction between the rollers and the specimen is simulated using coulomb friction with a friction coefficient of  $\mu = 0.05$ . The gripped regions on either end of the specimen are assumed to be rigid. Initially, both gripped regions are held stationary for a pre-strain CBT cycle. After the pre-strain cycle has been completed, a pull rate of 1.219 mm/s is applied to one side of the specimen. The pull rate of 1.219 mm/s governs a strain rate similar in magnitude to that in subsequent ST. It is selected to minimize the unavoidable discrepancy in testing conditions during pre-straining (CBT) and subsequent quasi-static testing (ST). Strain rate sensitivity of DP 780 is relatively low, which further minimize any bias in the identification of its post-necking strain hardening due to the strain rate and strain path changes.

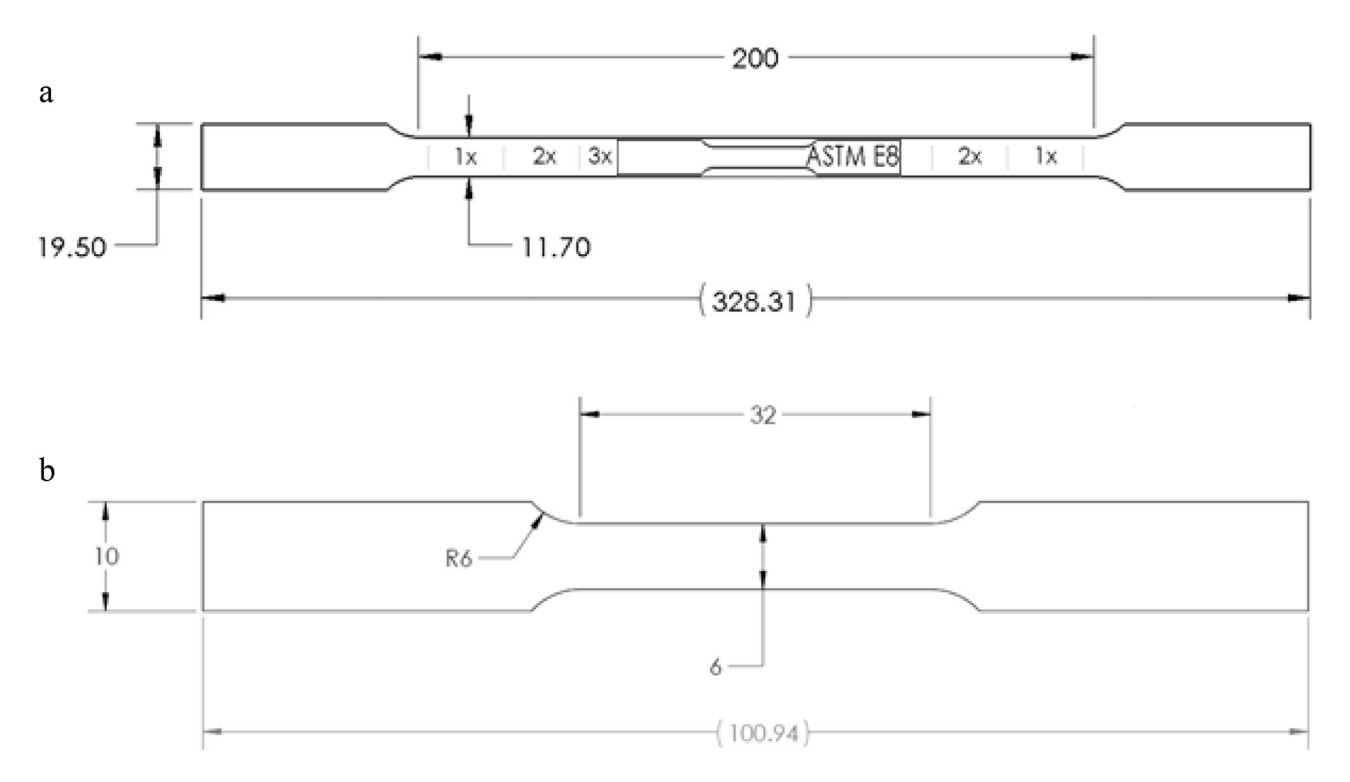


Fig. 2. (a) CBT specimen geometry with the  $1 \times, 2 \times$ , and  $3 \times$  regions and an ASTM E8 sub-size specimen for secondary simple tension (ST) testing. Thickness of the specimen is determined by the thickness of the sheet, which is 1.4 mm. (b) ASTM E8 sub-size specimen geometry for secondary ST testing. All dimensions are in mm.

The converged in-plane mesh with approximately 0.75 mm length of element edge was used for the CBT test simulations. The in-plane dimensions are refined enough to follow the profile of the rollers and to not influence appreciably the accuracy of the force versus displacement curve. The model had 7 elements through thickness to appropriately capture through-thickness profiles and 33,516 elements in total. The number of elements through thickness determines the accuracy of the bending stress profile and must be sufficiently refined in order to properly capture the distribution. Reduced integration linear elements (C3D8R) in bending are prone to a non-physical zero-energy mode of deformation referred to as hourglassing. In order to suppress this non-physical mode of deformation while maintaining a low amount of artificial strain energy added to the system, enhanced hourglass control was used.

In an effort to simulate the secondary ST as consistently with experiments as possible, the following automated procedure is developed. First, a 10 CBT cycles test is simulated. A python script is then used to restart the simulation at 2, 4, 6, 8, and 10 cycles to perform springback. The springback is modeled by applying a damping factor of  $2e^{-6}$  and releasing all contact constraints. The deformed shapes after springback are shown in Appendix A. To match the experimental procedure as closely as possible, each specimen is flattened following the springback simulations to allow for cutting of sub-size specimens. The flattening was accomplished by two plates pancaking the specimen in the displacement control. Next, mesh of each flattened specimen is converted to geometry using the built in geometry from mesh plugin. The geometries are then cut to create the sub-size specimen from each of the flattened model geometries using a Boolean operation. The sub-size geometries are meshed using approximately 100,000 C3D4 elements shown in Fig. 3e and f. The stress and plastic strain fields are mapped onto the cut parts from the flattened FE models for the subsequent ST simulations. Upon the ST simulations, the force versus displacement curves are extracted from each of the ST simulations and the strain-strain response is calculated the same way as done experimentally.

#### 5. Material models

The simulations of the CBT test for load versus displacement and the secondary ST for yield stress were carried out using IH and CIKH material models. Both models are available in Abaqus [54]. The rate-independent plasticity theory of von Mises (also known as  $J_2$ ) with a yield surface that can expand isotropically based on a given true stress-true strain curve. The given stress strain curve is the large strain flow curve for DP 780. For the CIKH model, the flow-rule is based on the plastic potential, f, with the plastic strain rate tensor derived as

$$\dot{\varepsilon}^p = \frac{\partial f(\sigma - \alpha)}{\partial \sigma} \dot{p} \tag{1}$$

with the following yield criterion

$$f(\boldsymbol{\sigma} - \boldsymbol{\alpha}) = J_2(\boldsymbol{\sigma} - \boldsymbol{\alpha}) - \sigma_o - R = \sqrt{\frac{3}{2}(\mathbf{s} - \mathbf{a}) : (\mathbf{s} - \mathbf{a})} - \sigma_o - R \tag{2}$$

and  $\sigma$  is the Cauchy stress tensor and  $\alpha$  is a back-stress tensor, while  $\mathbf{s}$  and  $\mathbf{a}$  are the corresponding deviatoric components. The remaining variables are  $\sigma_o$ , R, and  $\dot{p}$  are the initial yield stress, flow stress, and the equivalent plastic strain rate, respectively. The center of the yield surface is assumed to translate according to a 4-term Chaboche-type, non-linear kinematic hardening model [57] as

$$\alpha = \sum_{i=1}^{4} \alpha_i \tag{3}$$

with

$$\dot{\alpha}_{i} = C_{i} \ \dot{p} \ \frac{\sigma - \alpha}{\sigma_{o} + R} - \gamma_{i} \ \alpha_{i} \ \dot{p} \tag{4}$$

In Eq. (4),  $C_i$  and  $\gamma_i$  are fitting parameters. Finally, the yield surface evolves isotopically using an exponential law as

$$R = R_{max} \left( 1 - e^{-bp} \right) \tag{5}$$

where  $R_{max}$  is the maximum expansion of the yield surface and b is a parameter that controls the decay rate of the expansion of that surface.

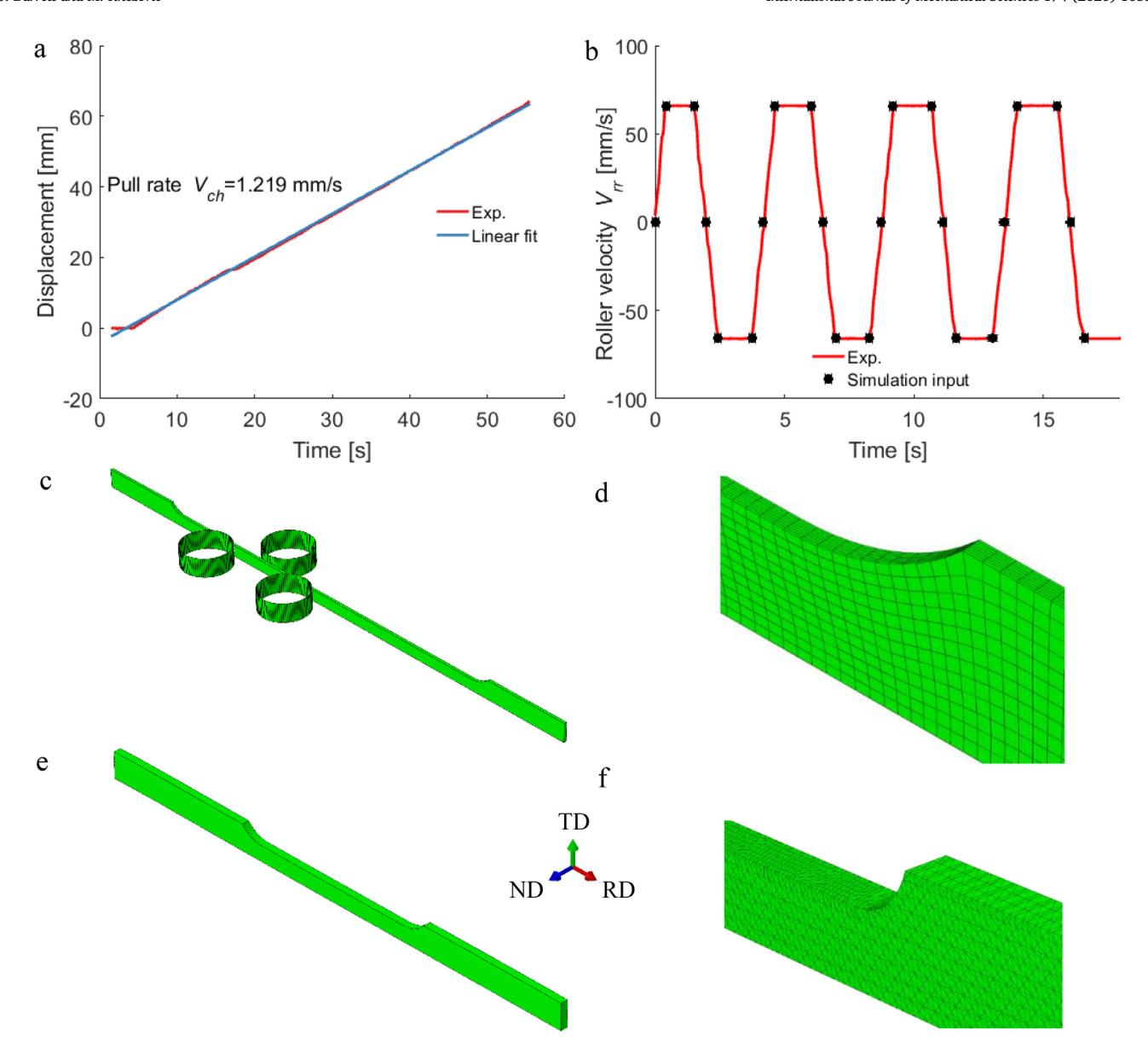
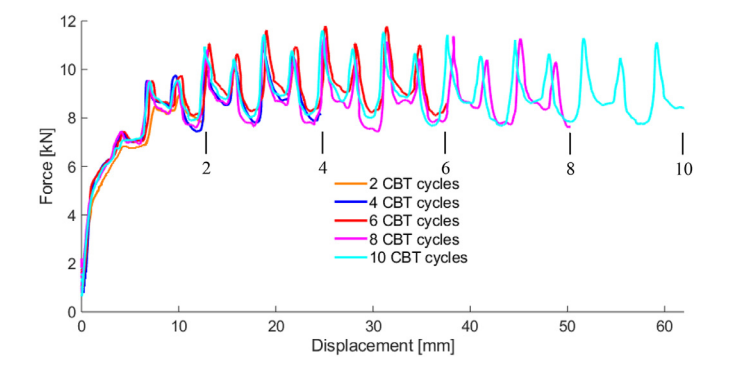


Fig. 3. Along with the bending depths of 2.6 mm, (a) measured displacement versus time resulting with the crosshead pull velocity of  $V_{CH} = 1.219$  mm/s and (b) roller velocity,  $|V_{rr}| \approx 66$  mm/s after acceleration/deceleration, versus time are CBT test parameters. As the carriage reciprocates during the CBT test, the positive values in the velocity profile imply the carriage motion in a given/forward direction, while the negative values indicate the carriage motion in the reverse/backward direction. (c) CBT finite element simulation setup with an insert showing mesh in (d). (e) Sub-size specimen model with an insert showing mesh in (f).

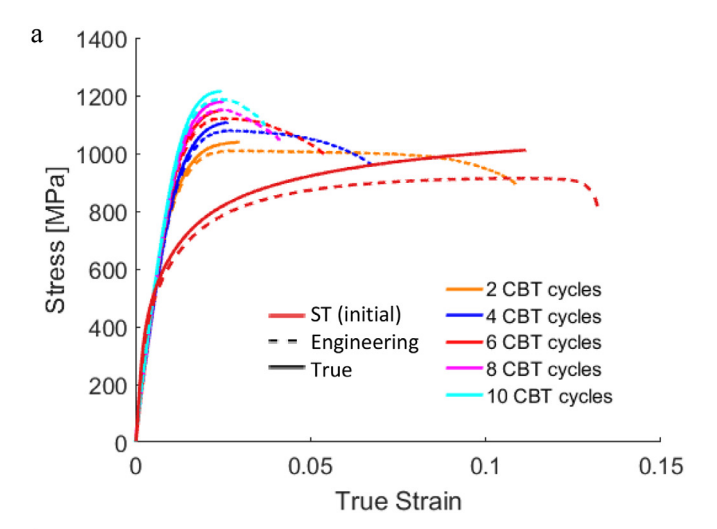
#### 6. Results

#### 6.1. Experimental measurements

Fig. 4 shows load versus displacement curves recorded during CBT testing along the rolling direction (RD) under a crosshead velocity of 1.219 mm/s, a bending depth of 2.6 mm, and a carriage velocity of 66 mm/s. The tests were interrupted at the specific number of CBT cycles and the specimens removed from the CBT testing device. Upon removal, the interrupted specimens were not straight like during testing but deflected. The free-state shape showed a certain amount of residual curvature. Appendix A presents photographs of the specimens in their free-state after testing to the given number of CBT cycles. As is evident, CBT introduces a slightly non-symmetric through-thickness stress profile governing the distortion. The combination of bending and ST leads to the tension versus compression asymmetry, where the neutral axis cyclically shifting towards the surface of the roller over which the sheet



**Fig. 4.** Force versus displacement curves for CBT tests along RD under a crosshead velocity of 1.219 mm/s, a bending depths of 2.6 mm, and a carriage velocity of 66 mm/s. Considering that the curves are approximately overlapping, their ends are indicated in the plot for clarity.



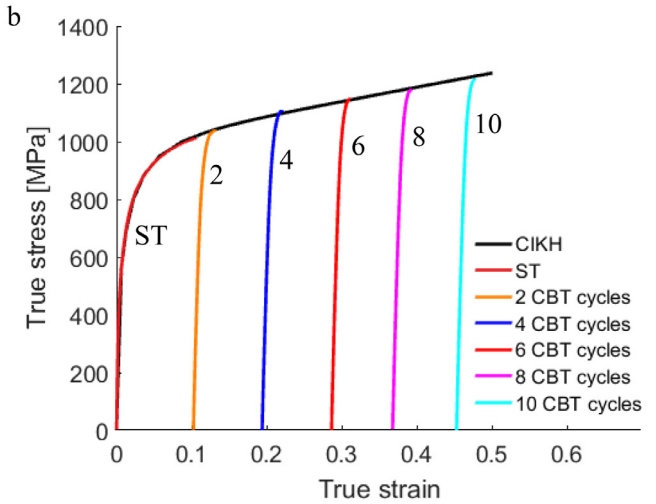


Fig. 5. (a) True stress-strain and engineering stress-strain curves of DP 780 recorded during secondary ST tests of sub-size specimens under a strain rate of  $0.001~\rm s^{-1}$  at room temperature along RD to the number of cycles indicated in the legend. The ST curve of the initial material is shown for reference. (b) Large strain (post-necking) flow curve for DP 780 based on shifting the secondary true stress-true strain curves from (a). The large strain flow curve (black color) is fitted using the Chaboche material model (CIKH).

is passing. The addition of bending stress profile to the tensile stress profile on the tension side governs that a lower force is required to reach the plastic flow stress of the material on the outward edge of the strip (relative to a roller) exposed to tension. Hence, the axial load versus displacement curve recorded in CBT is lower than that in ST [27]. As straightening of the distorted specimens could be done by hand, the non-symmetric residual stress in the specimens is relatively small. The distorted CBT specimens were flattened while fixtured in order to machine a sub-size ST specimen from each for secondary testing. The cutting was performed using the wire-electrical discharge machining (EDM) from the 3x deformation regions. After the sub-size specimens are released from the fixture, they deflect back. Strength of these pre-strained specimens can now be evaluated by secondary ST tests in order to infer the post-necking hardening behavior. Fig. 5a shows engineering and true stress versus strain curves based on the secondary ST tests. The ST tests were carried out under a strain rate of  $0.001 \text{ s}^{-1}$ . As is evident, the strength of the material increases with the CBT cycles, while the ETF decreases. Fig. 6 summarizes the evolution of elastic slope, yield strength, and strain at fracture for the tested specimens. Because of the initial non-linearity in stresses due to sample straightening, the elastic slope

**Table 2**True strain levels estimated analytically for the CBT samples of DP 780.

# of cycles	ε		
2	0.1025		
4	0.1941		
6	0.2864		
8	0.3679		
10	0.4531		

was measured from the curves between 100 MPa and 400 MPa. While ruling out the phenomena responsible for the reduction of the macroscopic elastic slope from the initial value for the DP 780 sheet to those after CBT treatment warrants further investigations, formation of backstress fields during CBT is the most likely mechanism responsible for it. Density of dislocations, especially geometrically necessary dislocations, increases heterogeneously with plastic deformation in CBT giving rise to such back-stress fields.

#### 6.2. Identification of large strain (post-necking) flow curve

Fig. 5b shows a large strain flow curve for DP 780 based on shifting the secondary true stress-true strain curves from Fig. 5a. Considering that the proposed approach does not yield an extrapolated strain hardening behavior as it is based on measurements, the text refers to the inferred flow curve as a 'large strain (post-necking) flow curve' or just as a 'large strain flow curve'. The accumulated strain during CBT in the 3x deformation region for the shifts is estimated as follows. As the sheet deforms incrementally at the locations being bent/unbent implies that only the material visited by the rolls elongates. As a result, the gauge length, l, of the CBT specimen is the length that the carriage delineates (i.e. the length of the roller stroke),  $l = \int V_{rr} dt$ . The specimen elongates as a consequence of the crosshead motion for  $dl \approx \Delta l = \int V_{CH} dt$ . The integrals are calculated numerically from the crosshead and roller velocity experimentally measured profiles. Thus, the average strain increment per pass,  $\Delta \varepsilon$ , is the ratio

$$\Delta \varepsilon = \int \frac{dl}{l} = \frac{\int V_{CH} dt}{\int V_{rr} dt} \tag{6}$$

The strain after a certain number of CBT cycles is a sum of the strain increments per pass. Table 2 presents the estimated strain levels for the CBT samples as a function of CBT cycles.

## 6.3. FEM analysis

We now turn our attention to the results of the FEM simulations. Here, the experimentally measured large strain flow curve is used as a guess to simulate the load versus displacement and secondary ST tests for the purpose of its validation. The curve is used directly as the input for the IH model, while the same curve is determined using the model parameters for the CIKH model. The CIKH model is calibrated using a set of experimentally measured large strain cyclic data for DP 780 [58] (Fig. 7a and b). The two cyclic experiments were selected to resemble the material behavior under CBT. Moreover, the calibrated model is simultaneously adjusted to reproduce the hardening responses (Fig. 5b), before using it in CBT simulations. The model parameters are given in Table 3. Fig. 8 shows a comparison between measured and predicted load versus displacement curves during the CBT testing. While both models are regarded to reproduce well the experimental curve, the IH model predicts a slightly softer response than the CIKH material model. This is attributed to a combination of the kinematic and isotropic evolution of the yield surface. To further verify the simulations, Table 4 presents comparisons between measured and predicted sheet thickness in the 3x deformation region after the testing. Both IH and CIKH predict

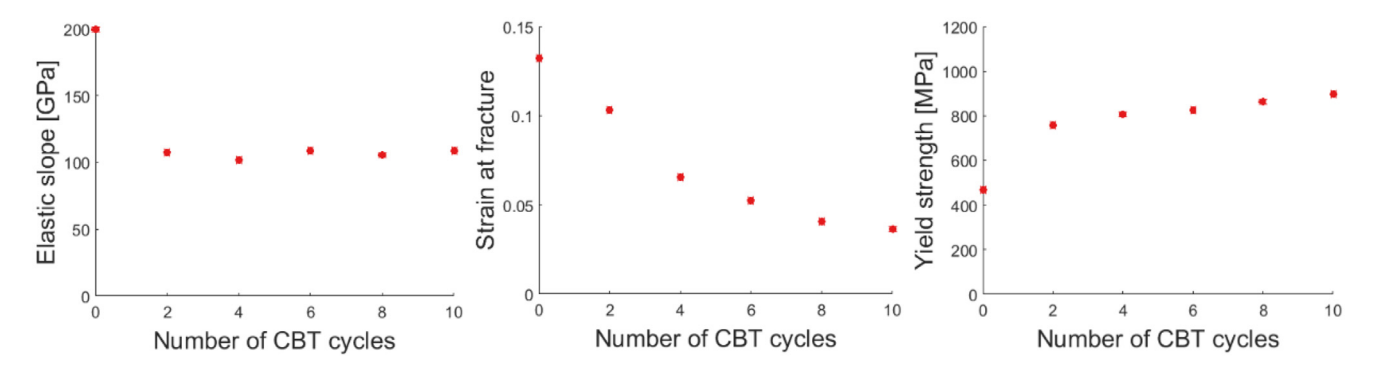


Fig. 6. Material properties of DP 780 based on the tests from Fig. 5. Yield strength is taken as a 0.2% offset. 0 CBT cycles corresponds to ST of the initial i.e. undeformed material.

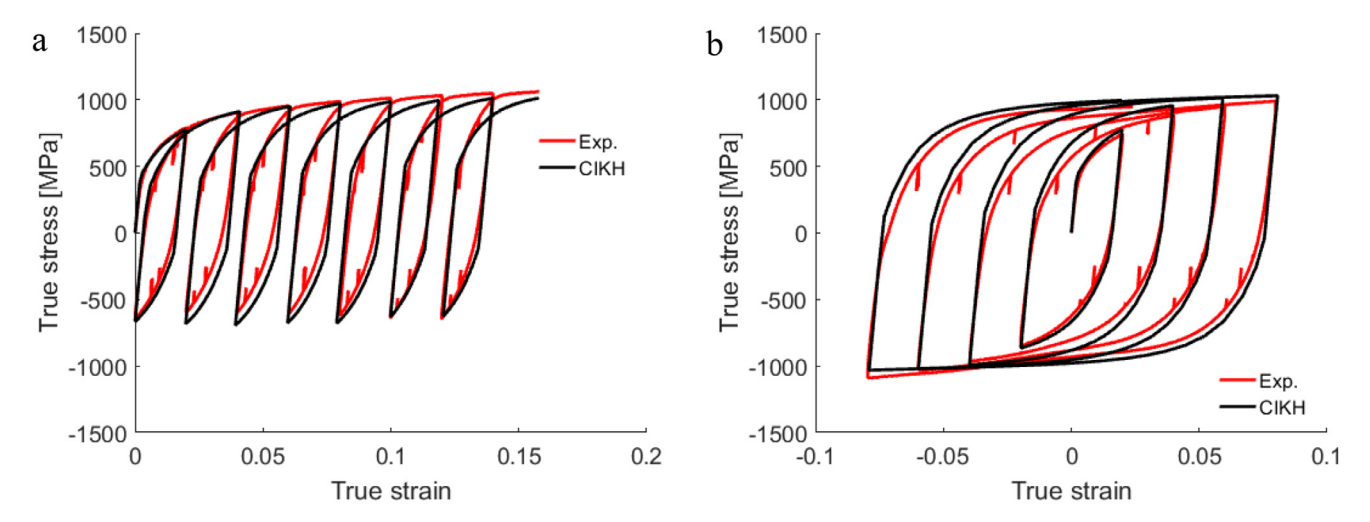


Fig. 7. Comparison of measured (Exp.) and fitted (using the CIKH model) true stress-true strain reversals for DP 780 along RD. The load reversal tests/simulations were performed following two strain paths (logarithmic strain): (a)  $0 \rightarrow 0.02 \rightarrow 0.04 \rightarrow 0.04 \rightarrow 0.02 \rightarrow 0.06...$  up to fracture and (b)  $0 \rightarrow 0.02 \rightarrow -0.02 \rightarrow 0.04 \rightarrow -0.04 \rightarrow 0.06...$  up to fracture.

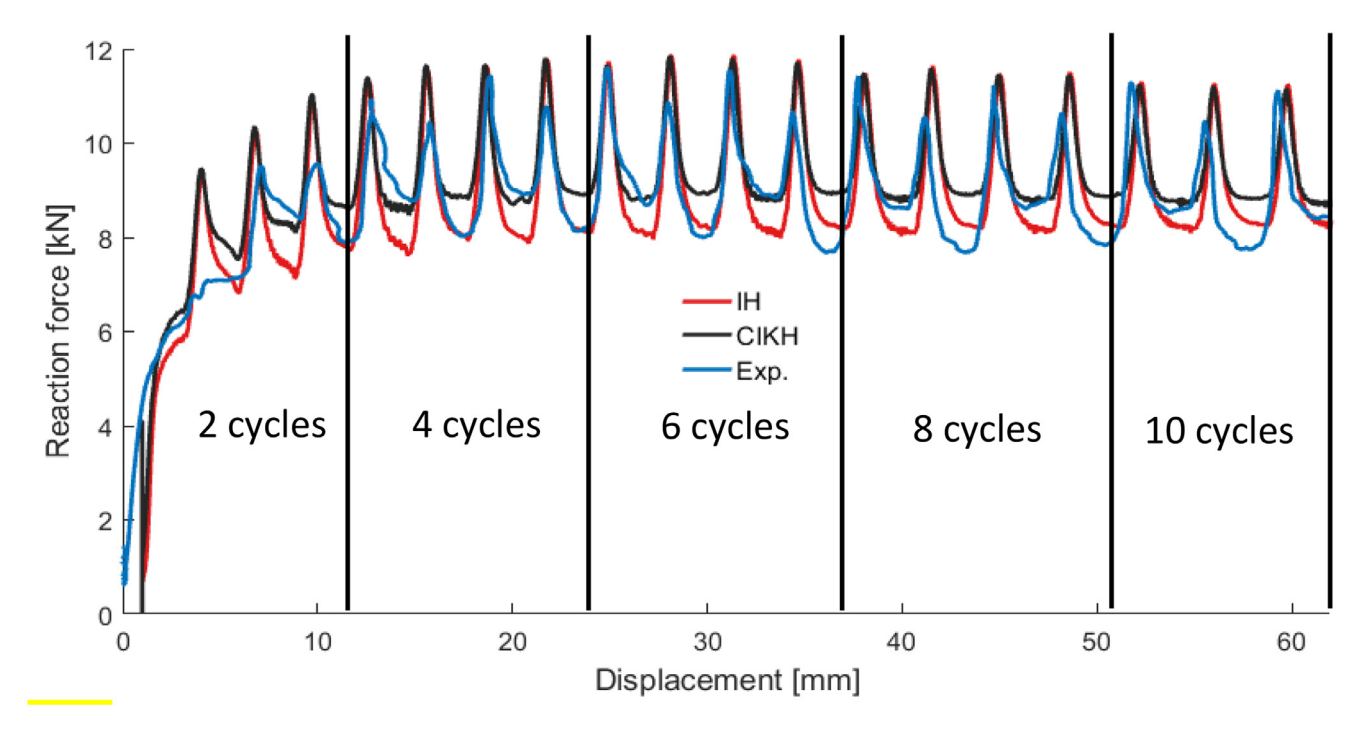


Fig. 8. Force versus displacement recorded during a CBT experiment along RD under a crosshead velocity of 1.219 mm/s, a bending depths of 2.6 mm, and a carriage velocity of 66 mm/s as compared to equivalent simulation results using IH and CIKH material models.

**Table 3**CIKH model parameters for DP 780. Young's modulus and Poisson's ratio are 207,325 MPa and 0.3, respectively.

$\sigma_o$ [MPa]	420
$C_1$ [MPa]	20000
$C_2$ [MPa]	15000
$C_3$ [MPa]	9000
$C_4$ [MPa]	490
$\gamma_1$	200
$\gamma_2$	107
γ <sub>3</sub>	46
γ <sub>4</sub>	0
$R_{\rm max}$ [MPa]	140
b	18

**Table 4**Measured and predicted sheet thickness in the 3x deformation region during the testing.

Cycle #	Predicted thickness [mm]	Measured thickness [mm]
2	1.35	1.37
4	1.28	1.28
6	1.22	1.21
8	1.16	1.13
10	1.12	1.08

approximately the same thickness. The measurements were performed using a micrometer at several locations. Average values are calculated and presented in the table. The difference is small verifying the predictions.

As Fig. 3b shows, the carriage repeatedly accelerates linearly at the beginning of each pass, which is followed by the constant velocity for an extended period of the pass, and finally decelerates linearly. The load spikes form during the deceleration-to-stop/acceleration-to-maximum velocity periods. At the stop of the carriage, the bending is paused for a moment, while the stress state in the specimen approaches the ST condition. As a result, the force raises. As soon as the carriage starts moving again, the bending resumes dropping the load. The plateaus between peaks is nearly a steady state condition as a consequence of constant velocity. Note also a small difference between the load magnitudes for every other plateau for the experimental curve. In one case, the material is moving towards (lower load), while in the other case, the material is moving away (higher load) from the load recording load cell. These effects are not captured well in the simulations.

The developed simulation procedure accounting for distortions due to the evolution of the residual stress fields during CBT and secondary ST is used for the FEM simulations. The stages in the simulation process being carried out are shown in Fig. 9. The example is illustrated for 2 CBT cycles. Fig. 9a-d are of the full size CBT specimen, while Fig. 9e-h are of the sub-size specimen. The figure showing the initial specimen is repeated in Fig. 9a. The clamped specimen after 2 CBT cycles is shown in Fig. 9b. The deflected CBT specimen after it is removed from the grippes is shown in Fig. 9c. The 3x deformation region nodal coordinates of the FE model were output, a fourth order polynomial is fit to the nodes, and two derivatives are taken to calculate the curvature of the specimen. The same analyses was done using the images of experimentally deformed specimens. These specimens after the deflection are shown in Appendix A. A comparisons between the measured and simulated curvatures with IH model for CBT samples is shown in Fig. 10. The magnitude and trends are reproduced reasonably well using the numerical models. The specimen is flattened before cutting (Fig. 9d). The cutting of the FE mesh into the sub-size specimen shape is accomplished by Boolean operations in Abaqus followed by generation of volume FE mesh and mapping of the state variables (Fig. 9e). During cutting, the sub-size specimen distorts as it is removed, while the stress fields evolve

**Table 5**Strain levels based in Eq. (6) and the FEM simulations (PEEQ is the effective strain, LE11 is the axial strain component) versus the number of cycles.

# of cycles	ε	PEEQ	LE11
2	0.1025	0.0999	0.0941
4	0.1941	0.1911	0.1813
6	0.2864	0.2728	0.2612
8	0.3679	0.3543	0.3417
10	0.4531	0.424	0.4003

to reach a new equilibrium. The state variables were necessary to be mapped because of simulating the evolution of the residual stress field to a new equilibrium, which is accompanied by the deflection (Fig. 9f). Finally, the sub-size specimens were tested by superimposing ST over the residual stress (Fig. 9g and h).

Fig. 11 shows a comparison between measured and predicted flow stress curves based on the secondary ST tests as well as the evolution of the elastic slope and yield strength. Apparent elastic slopes after the CBT pre-deformation steps are reduced relative to the initial material. The reduction is driven by the residual stress state introduced into the material by CBT testing. As is evident from the early portion of the curves in Fig. 11, the stress required for straightening of the samples is very small. The initial non-linearity during loading using the IH material model is due to the spingback effects and straightening of the sub-size specimen. The implications are negative strains at the beginning of the ST tests. The springback effects appear much smaller based on the CIKH material model as the negative strains and the non-linearity at low strain levels are small. However, the CIKH model is able to capture well the work hardening during the secondary tests of the material due to shifting of the yield surface. Moreover, since points throughout the thickness of the material yield at different stress levels the subsequent deformation is more stable. Considering that the yielding of the samples is well captured by the models, these results are regarded to further verify the experimentally measured large strain flow curve. Note that the experimental data does not exhibit the initial non-linearity since the specimens were forcefully straightened prior to the beginning of ST testing.

Table 5 presents a comparison between estimated strain levels used to shift the curves using Eq. (6) and the FEM simulations versus the number of cycles. The FEM strains are integrated over the 3x deformation region. Considering that the effective strain (PEEQ) and the axial strain component (LE11) strain measures are similar in magnitude confirms the uniaxial stress/strain state in the material during CBT. Moreover, the similarity between the effective von Mises stress and the axial stress component contours further confirms the uniaxial state of the mechanical fields in the material. It is also worth mentioning that texture evolution in CBT is about the same as the texture evolution under ST. This is again because of approximately the same strain state in the material deformed under CBT and ST. These results have been presented in our earlier works [50].

#### 7. Discussions

In this work, a systematic methodology to infer the material behavior at large plastic strains is presented and verified. The methodology is based on a combination of experiments and FEM analysis. The experiments involve a set of CBT tests to pre-strain specimens and secondary ST testing of the pre-strained material to approximate the post-necking behavior. The FEM simulations pertain to verification by comparing the simulation results and experiments in terms of the CBT load versus displacement curves and secondary ST flow curves. Such methodology is needed to approximate large strain material behavior because many sheet metal forming operations impart such high levels of plastic strain. To facilitate accurate FEM simulations of those forming operations, the material behavior at the required high strain levels must be known.

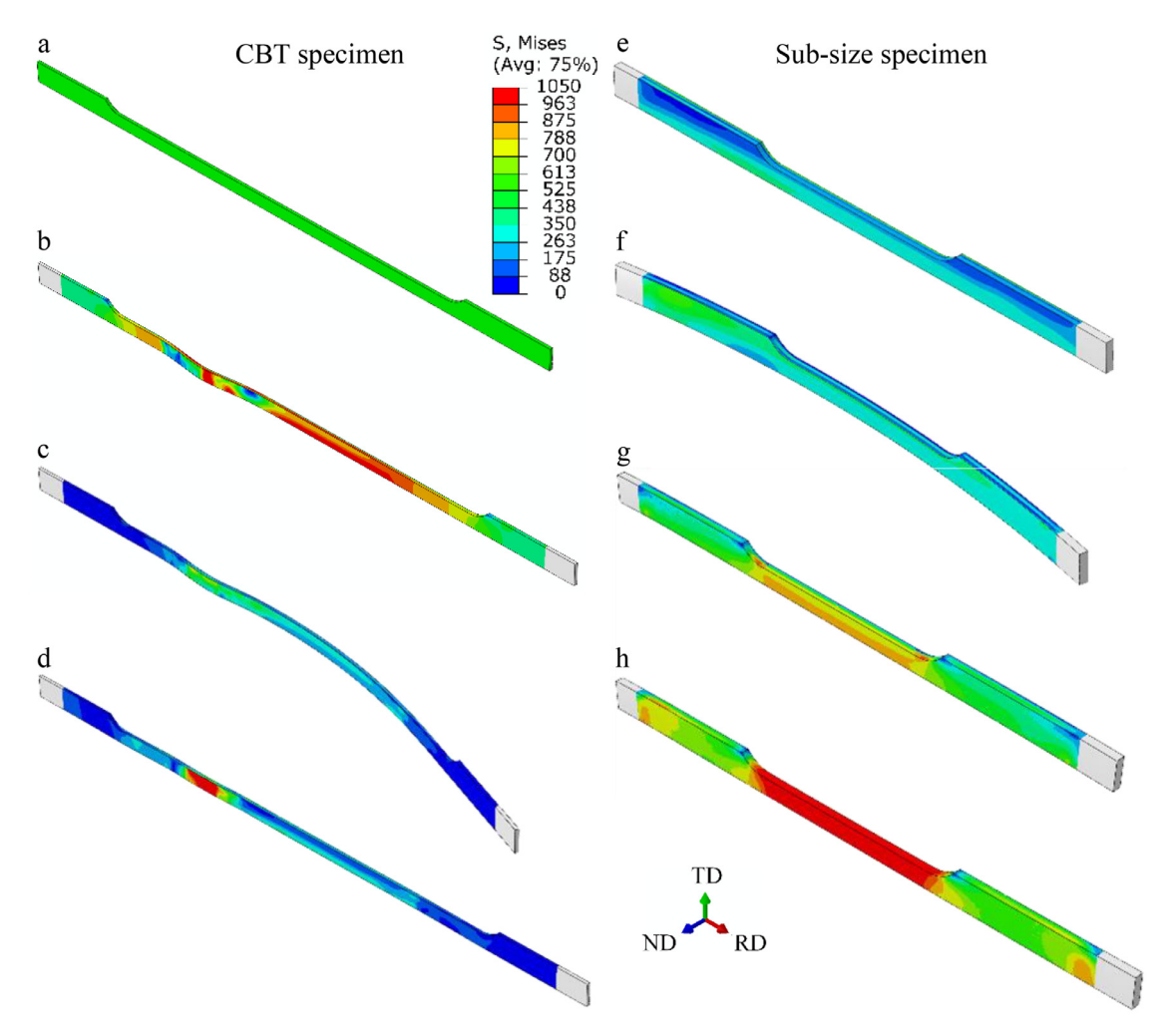
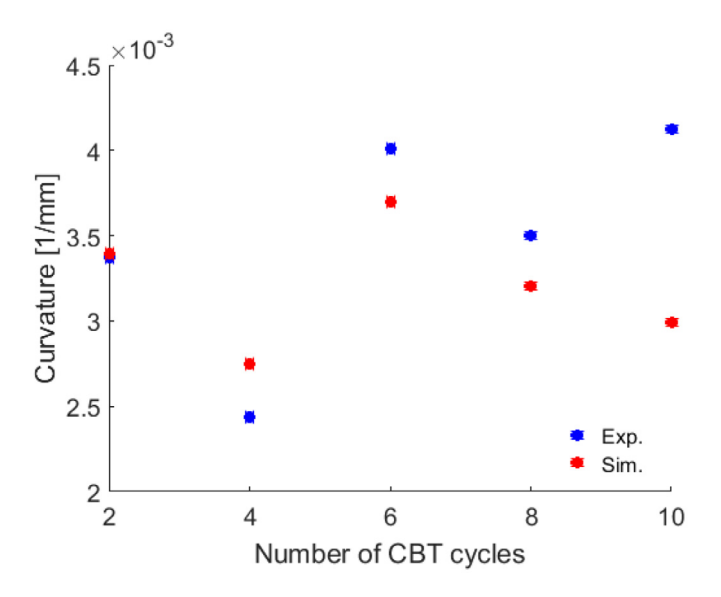


Fig. 9. Stages throughout the interrupted testing procedure: (a) an initial CBT specimen, (b) the specimen after 2 CBT cycles, (c) the specimen after springback, (d) the specimen after straightening, (e) a sub-size specimen cut from the specimen in (d), (f) the sub-size specimen after springback, (g) the sub-size specimen after straightening, and h) the sub-size specimen during subsequent tension test.



**Fig. 10.** Comparison of measured and simulated using the IH model springback curvature for the CBT tests as a function of CBT cycles. Appendix A shows the corresponding images of the measured specimens and those simulated by the IH model.

The strain levels in the CBT test substantially exceed the strain levels achieved inside the neck of a specimen tested in ST [27], facilitating the development of the extrapolation methodology. Strength of the material increases with the number of CBT cycles. Thus, the hardening curve that is input in the FEM simulations of CBT must be existing past the limit of uniform elongation in ST. The CBT test depletes ductility uniformly throughout the gauge section of a tested sheet, and thus, stretches the sheet far beyond the point of maximum uniform strain in a ST test. The developed methodology is used to identify the post-necking hardening behavior of DP 780 steel. The hardening curve of the material is measured experimentally based on the curves obtained using the secondary ST of pre-deformed samples in CBT. The secondary flow curves are appropriately shifted for the amount of pre-strain accumulated during CBT within the 3x deformation region. The accumulated strain levels are estimated using an analytical approach, which is verified later using the FEM simulations.

The inferred curve is validated by confirming that the predicted crosshead load versus displacement curves match the experimental ones. The simulated load versus displacement curves based on the IH and CIKH material models are in good agreement with the measured data implying that the method can be used to extract post-necking material behavior. As the hardening curve used for the IH simulation case is identical to that of the CIKH case, the predictions were similar. Since so, the amount of kinematic hardening effects exhibited by the material under CBT is small to moderate. Significantly, the method can facilitate

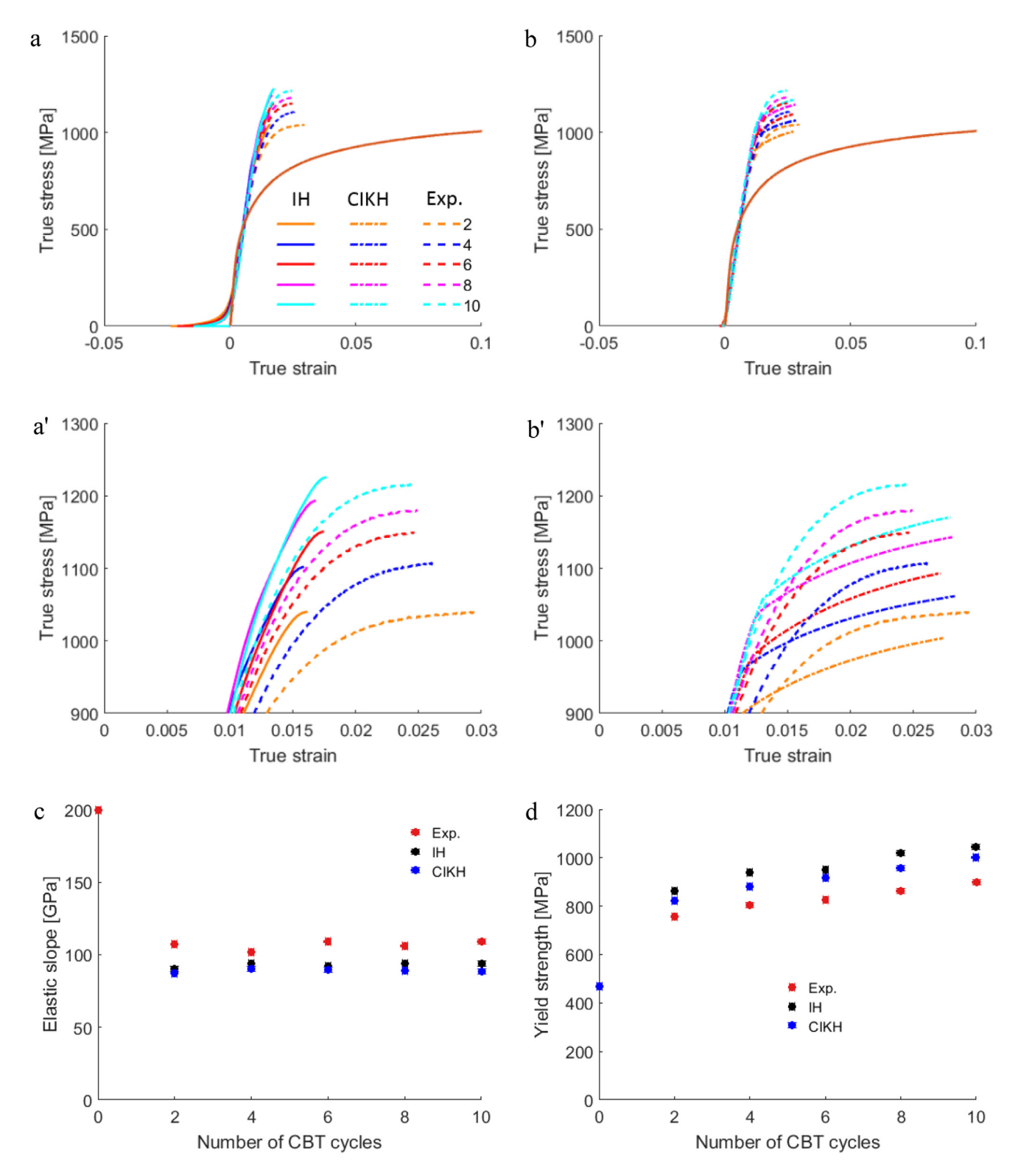


Fig. 11. Comparison of measured and predicted using (a) IH with zoomed in on yielding (a') and (b) CIKH with zoomed in on yielding (b') true stress-true strain curves based on secondary ST tests for DP 780 samples after 2, 4, 6, 8 and 10 CBT cycles. 0 cycles corresponds to ST for the initial material. (c) Elastic slope and (d) yield strength defined by 0.2% offset based on the curves in (a) and (b).

determining the evolution of anisotropy to large plastic strains because it can be applied in any sample direction. Favorable comparison between measured and simulated sheet thickness in Table 4 is also an additional verification for the simulations. Furthermore, the experimentally measured curve is validated by comparing measured and predicting yield

stress based on the secondary ST tests. To simulate these tests accurately and efficiently, an automated procedure involving the deflection simulations is developed and implemented in Abaqus. These simulations were also performed using both the IH and CIKH material models. The CIKH model was found to better stabilize the secondary ST simulation

and to slightly better predict the material behavior than the IH model at higher strains. Good predictions indicate that the extension of the hardening curve using the secondary ST testing of pre-deformed CBT samples is a sound methodology to infer the material behavior at high strain levels. While the overall methodology combining CBT and FEM can facilitate further adjusting of the post-necking hardening curve to better reproduce the experimental data, the initially guessed curve was regarded as accurate as the measured and simulated data were in good agreement. As the curves derived from secondary ST tests can be fit in a large strain flow curve, which is further verified with the simulations, we rationalize that the level of hardening during CBT is as not significantly affected by the bending cycles but mainly by the accumulated length strain, as suggested by the earlier works.

In closing, we would like to point out that the performed simulations are regarded to capture the measured data reasonably well, considering the simple IH  $J_2$  plasticity and more accurate CIKH constitutive descriptions of the material. The predictions could be further improved by involving more accurate material models such as those based on crystal plasticity theory incorporating the kinematic hardening effects [59–63]. Future works will attempt to simulating the diffuse neck in the ST using the identified large strain flow curve as well as for further validation compare the identified strain hardening curve with the one obtained from a bulge test. Finally, we point out that the methodology developed here would need further developments if a material would exhibit different hardening characteristics under CBT than ST. If the strength of a material appears to be driven by achieved heterogeneous microstructure meaning that the achieved effective strain level is insufficient to characterize the state of the material then the strength measured by CBT may not be a reliable way to determine large strain flow curves. However, if these effect occur lowering the bend depth is the way to minimize the bending effects and come closer to ST.

## 8. Conclusion

This paper presented a combined experimental and simulation methodology to identify post-necking hardening behavior of ductile sheet metals. The method is used to successfully identify the post-

necking hardening behavior of DP 780 steel. A set of DP 780 CBT samples are pre-deformed to several strain levels greater than the necking strain level by interrupting their CBT testing. Sub-size specimens are machined by EDM from the CBT interrupted specimens and tested in ST. The flow curves from these secondary ST tests are then shifted for the levels of axial strain accumulated during pre-deformation by CBT to determine a large strain flow curve of the material. The experimentally identified large strain curve is validated by simulations performed using the IH and CIKH material models reproducing the curve. The latter model is calibrated using a suitably selected set of large strain cyclic tension-compression data for modeling of CBT. The FEM simulation pertain to verification of the curve by comparing the simulation results and experiments in terms of the CBT load versus displacement curves and secondary ST flow curves. It is found that the model reproduces the experimental load versus displacement curve, including the succession of spikes and plateaus typical of CBT, very closely. The model also predicts yielding of the interrupted sub-size specimens further verifying the identified curve. Good predictions testify that the developed methodology can be used for inferring hardening curves at high strain levels for sheet metals. It is shown that the strength is unaffected by the cyclic predeformation but primarily depends on the overall increase in length.

#### **Declaration of Competing Interest**

The authors declare that they have no known competing financial interests or personal relationships that could have appeared to influence the work reported in this paper

#### Acknowledgments

This research was sponsored by the U.S. National Science Foundation and was accomplished under the CAREER grant no. CMMI-1650641.

## Appendix A

Fig. A2

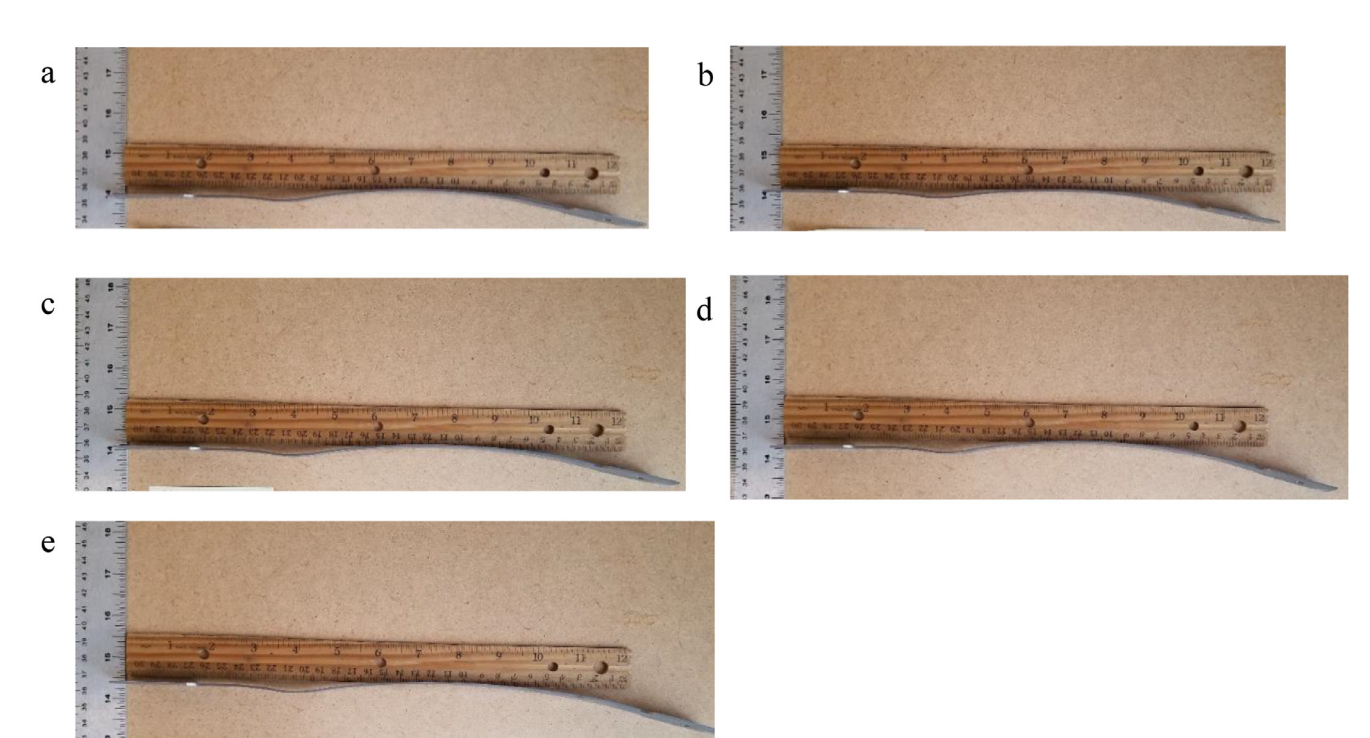


Fig. A1. Photographs showing deformed shapes of the tested CBT specimens in their free-state after (a) 2, (b) 4, (c) 6, (d) 8, and (e) 10 CBT cycles.

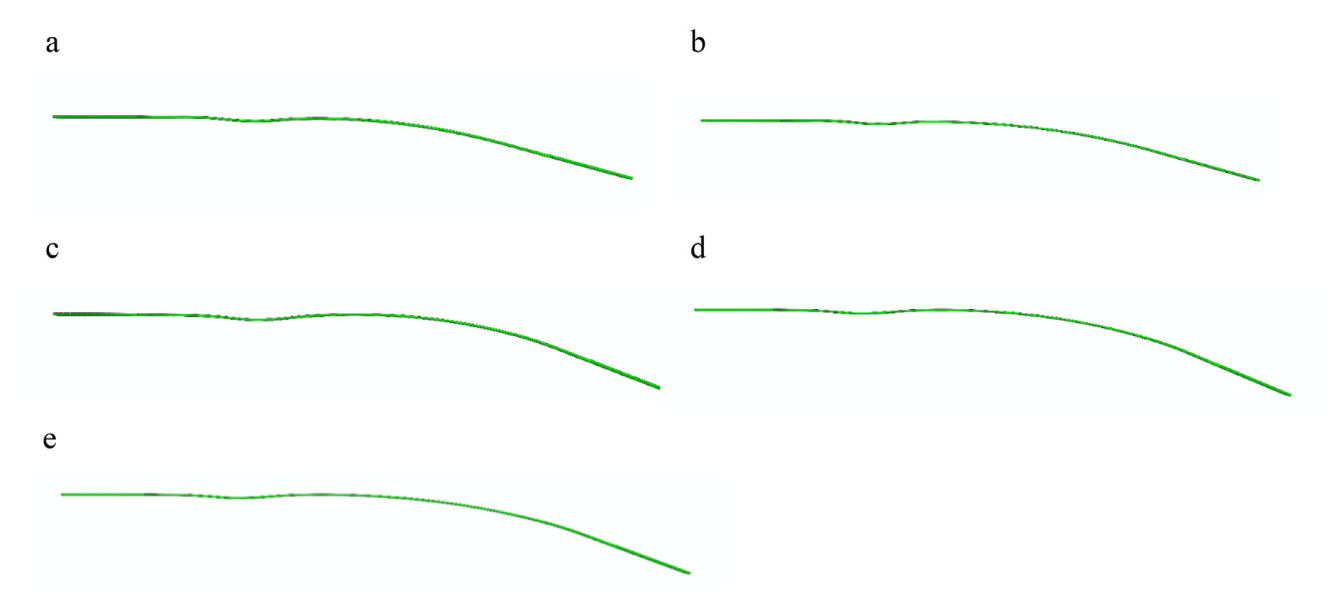


Fig. A2. FEM models after springback corresponding to the photographs in Fig. A1.

#### References

- [1] Barrett TJ, Knezevic M. Deep drawing simulations using the finite element method embedding a multi-level crystal plasticity constitutive law: experimental verification and sensitivity analysis. Comput Methods Appl Mech Eng 2019;354:245-70.
- [2] Knezevic M, Lebensohn RA, Cazacu O, Revil-Baudard B, Proust G, Vogel SC, et al. Modeling bending of  $\alpha$ -titanium with embedded polycrystal plasticity in implicit finite elements. Mater Sci Eng A 2013;564:116-26.
- [3] Jahedi M, Knezevic M, Paydar M. High-pressure double torsion as a severe plastic deformation process: experimental procedure and finite element modeling. J Mater Eng Perform 2015;24:1471-82.
- [4] Jahedi M, Paydar MH, Zheng S, Beyerlein IJ, Knezevic M. Texture evolution and enhanced grain refinement under high-pressure-double-torsion. Mater Sci Eng A
- [5] Hosford WF, Caddell RM. Metal forming: mechanics and metallurgy. New York, USA: Cambridge University Press; 2011.
- [6] Knezevic M, McCabe RJ, Lebensohn RA, Tomé CN, Liu C, Lovato ML, et al. Integration of self-consistent polycrystal plasticity with dislocation density based hardening laws within an implicit finite element framework: application to low-symmetry metals. J Mech Phys Solids 2013;61:2034-46.
- [7] Zecevic M, Knezevic M. Latent hardening within the elasto-plastic self-consistent polycrystal homogenization to enable the prediction of anisotropy of AA6022-T4 sheets. Int J Plast 2018:105:141-63.
- [8] Bridgman PW. Studies in large plastic flow and fracture. New York: McGraw-Hill;
- [9] Pottier T, Toussaint F, Vacher P. An inverse method for material parameters determination of titanium samples under tensile loading. Int J Mater Form 2008;1:21-4.
- [10] Kajberg J, Lindkvist G. Characterisation of materials subjected to large strains by inverse modelling based on in-plane displacement fields. Int J Solids Struct 2004;41:3439-59.
- [11] Tardif N, Kyriakides S. Determination of anisotropy and material hardening for aluminum sheet metal. Int J Solids Struct 2012;49:3496-506.
- [12] Knysh P, Korkolis YP. Identification of the post-necking hardening response of rateand temperature-dependent metals. Int J Solids Struct 2017;115-116:149-60.
- [13] Knezevic M, Crapps J, Beyerlein LJ, Coughlin DR, Clarke KD, McCabe RJ. Anisotropic modeling of structural components using embedded crystal plasticity constructive laws within finite elements. Int J Mech Sci 2016;105:227-38.
- [14] Savic V, Hector L, Snavely K. Effects of gauge section geometry on tensile material properties by digital image correlation. SAE Int 2012.
- Coppieters S, Kuwabara T. Identification of post-necking hardening phenomena in **[15]** ductile sheet metal. Exp Mech 2014;54:1355-71.
- [16] Rossi M, Pierron F. Identification of plastic constitutive parameters at large defor-
- mations from three dimensional displacement fields. Comput Mech 2012;49:53-71. Kim J-H, Serpantié A, Barlat F, Pierron F, Lee M-G. Characterization of the postnecking strain hardening behavior using the virtual fields method. Int J Solids Struct 2013;50:3829-42.
- [18] Grédiac M, Pierron F. Applying the virtual fields method to the identification of elasto-plastic constitutive parameters. Int J Plast 2006;22:602-27.
- [19] Avril S, Pierron F, Pannier Y, Rotinat R. Stress reconstruction and constitutive parameter identification in plane-stress elasto-plastic problems using surface measurements of deformation fields. Exp Mech 2008:48:403-19.
- [20] Coppieters S, Cooreman S, Sol H, Van Houtte P, Debruyne D. Identification of the post-necking hardening behaviour of sheet metal by comparison of the internal and external work in the necking zone. J Mater Process Technol 2011;211:545-52.

- [21] Barlat F, Glazov M, Brem J, Lege D. A simple model for dislocation behavior, strain and strain rate hardening evolution in deforming aluminum alloys. Int J Plast 2002:18:919-39.
- [22] Campos H, Santos AD, Martins B, Ito K, Mori N, Barlat F. Hydraulic bulge test for stress-strain curve determination and damage calibration for Ito-Goya model. In: 11th World Congress on Computational Mechanics, 5th European Conference on Computational Mechanics and 6th European Conference on Computational Fluid Dynamics; 2014. p. 4223-38.
- [23] Sevillano JG, Van Houtte P, Aernoudt E. Large strain work hardening and textures. Prog Mater Sci 1980;25:69-134.
- [24] Venet G, Balan T, Baudouin C, Bigot R. Direct usage of the wire drawing process for large strain parameter identification. Int J Mater Form 2019;12:875-88
- [25] Hering O, Kolpak F, Tekkaya AE. Flow curves up to high strains considering load reversal and damage. Int J Mater Form 2019;12:955-72.
- [26] Benedyk J, Parikh N, Stawarz D. A method for increasing elongation values for ferrous and nonferrous sheet metals. J Mater 1971;6:16-29.
- [27] Poulin CM, Korkolis YP, Kinsey BL, Knezevic M. Over five-times improved elongation-to-fracture of dual-phase 1180 steel by continuous-bending-under-tension. Mater Des 2019;161:95-105.
- [28] Poulin CM, Vogel SC, Korkolis YP, Kinsey BL, Knezevic M. Experimental studies into the role of cyclic bending during stretching of dual-phase steel sheets. Int J Mater Form 2020. doi:10.1007/s12289-019-01530-2.
- [29] Emmens WC. Formability: a review of parameters and processes that control, limit or enhance the formability of sheet metal. Berlin/Heidelberg, Germany: Springer;
- [30] Gribbin S, Bicknell J, Jorgensen L, Tsukrov I, Knezevic M. Low cycle fatigue behavior of direct metal laser sintered Inconel alloy 718. Int J Fatigue 2016;93(Part 1):156-67.
- [31] Gribbin S, Ghorbanpour S, Ferreri NC, Bicknell J, Tsukrov I, Knezevic M. Role of grain structure, grain boundaries, crystallographic texture, precipitates, and porosity on fatigue behavior of Inconel 718 at room and elevated temperatures. Mater Charact 2019;149:184-97.
- [32] Emmens WC, van den Boogaard AH. Cyclic stretch-bending: mechanics, stability and formability. J Mater Process Technol 2011;211:1965-81.
- [33] Emmens W, van den Boogaard AH. Material characterization at high strain by adapted tensile tests. Exp Mech 2012;52:1195-209.
- [34] Hadoush A, van den Boogaard AH, Emmens W. A numerical investigation of the continuous bending under tension test. J Mater Process Technol 2011:211:1948-56.
- [35] Barrett TJ, Savage DJ, Ardeljan M, Knezevic M. An automated procedure for geometry creation and finite element mesh generation: application to explicit grain structure models and machining distortion. Comput Mater Sci 2018;141:269–81.
- [36] M. Knezevic, B.K. Chun, J.Y. Oh, W.T. Wu, R.A. Ress Iii, M.G. Glavicic, S. Srivatsa, Modeling machining distortion using the finite element method: application to engine disk, in, 2012, pp. 40-46.
- [37] Calcagnotto M, Ponge D, Raabe D. Microstructure control during fabrication of ultrafine grained dual-phase steel: characterization and effect of intercritical annealing parameters, ISIJ Int 2012;52:874-83.
- [38] Woo W, Em VT, Kim EY, Han SH, Han YS, Choi SH. Stress-strain relationship between ferrite and martensite in a dual-phase steel studied by in situ neutron diffraction and crystal plasticity theories. Acta Mater 2012;60:6972-81.
- Gong H, Wang S, Knysh P, Korkolis YP. Experimental investigation of the mechanical response of laser-welded dissimilar blanks from advanced- and ultra-high-strength steels. Mater Des 2016;90:1115-23.

- [40] Ma B, Liu ZG, Jiang Z, Wu X, Diao K, Wan M. Prediction of forming limit in DP590 steel sheet forming: an extended fracture criterion. Mater Des 2016:96:401–8.
- [41] Ghaei A, Green DE, Aryanpour A. Springback simulation of advanced high strength steels considering nonlinear elastic unloading-reloading behavior. Mater Des 2015;88:461-70
- [42] Tasan CC, Hoefnagels JPM, Diehl M, Yan D, Roters F, Raabe D. Strain localization and damage in dual phase steels investigated by coupled in-situ deformation experiments and crystal plasticity simulations. Int J Plast 2014;63:198–210.
- [43] Kapp M, Hebesberger T, Kolednik O. A micro-level strain analysis of a high-strength dual-phase steel. Int J Mater Res 2011;102:687–91.
- [44] Wagoner RH, Kim JH, Sung JH. Formability of advanced high strength steels. Int J Mater Form 2009;2:359.
- [45] Bhadeshia HKDH. TRIP-assisted steels? ISIJ Int 2002;42:1059-60.
- [46] Shi M, Gelisse S. Issues on the AHSS forming limit determination. In: Proceedings of the IDDRG International Conference; 2006. p. 19–21.
- [47] Nikhare C, Hodgson P, Weiss M. Necking and fracture of advanced high strength steels. Mater Sci Eng. A 2011;528:3010–13.
- [48] Saeidi N, Ashrafizadeh F, Niroumand B, Barlat F. EBSD study of micromechanisms involved in high deformation ability of DP steels. Mater Des 2015;87:130–7.
- [49] Xue X, Liao J, Vincze G, Sousa J, Barlat F, Gracio J. Modelling and sensitivity analysis of twist springback in deep drawing of dual-phase steel. Mater Des 2016;90:204–17.
- [50] Zecevic M, Roemer T, Knezevic M, Korkolis Y, Kinsey B. Residual ductility and microstructural evolution in continuous-bending-under-tension of AA-6022-T4. Materials (Basel) 2016;9:130.
- [51] Roemer TJ. Experimental apparatus for continuous-bending-under-tension and experiments on AA6022-T4. Mech. Eng. Durham, NH. University of New Hampshire; 2016.
- [52] Roemer TJ, Barrett TJ, Knezevic M, Kinsey BL, Korkolis YP. Experimental study of continuous-bending-under-tension of AA6022-T4. J Mater Process Technol 2019;266:707-14.

- [53] Standard Test Methods for Tension Testing of Metallic Materials West Conshohocken, PA ASTM International: 2015.
- [54] . ABAQUS version 6. Providence, RI, USA: Dassault Systèmes; 2017.
- [55] Ardeljan M, Knezevic M. Explicit modeling of double twinning in AZ31 using crystal plasticity finite elements for predicting the mechanical fields for twin variant selection and fracture analyses. Acta Mater 2018;157:339–54.
- [56] Ardeljan M, Beyerlein IJ, Knezevic M. Effect of dislocation density-twin interactions on twin growth in AZ31 as revealed by explicit crystal plasticity finite element modeling. Int J Plast 2017;99:81–101.
- [57] Chaboche JL. Time-independent constitutive theories for cyclic plasticity. Int J Plast 1986;2:149–88.
- [58] Daroju S, Maeda T, Kuwabara T, Knezevic M. Experimental characterization and crystal plasticity modeling of dual-phase steels subjected to strain path reversals. Int J Plast 2020.
- [59] Zecevic M, Korkolis YP, Kuwabara T, Knezevic M. Dual-phase steel sheets under cyclic tension-compression to large strains: experiments and crystal plasticity modeling. J Mech Phys Solids 2016;96:65–87.
- [60] Cantara AM, Zecevic M, Eghtesad A, Poulin CM, Knezevic M. Predicting elastic anisotropy of dual-phase steels based on crystal mechanics and microstructure. Int J Mech Sci 2019;151:639–49.
- [61] Eghtesad A, Knezevic M. High-performance full-field crystal plasticity with dislocation-based hardening and slip system back-stress laws: application to modeling deformation of dual-phase steels. J Mech Phys Solids 2020;134:103750.
- [62] Knezevic M, Beyerlein IJ, Lovato ML, Tomé CN, Richards AW, McCabe RJ. A strain-rate and temperature dependent constitutive model for BCC metals incorporating non-Schmid effects: application to tantalum-tungsten alloys. Int J Plast 2014;62:93-104.
- [63] Zecevic M, Knezevic M. An implicit formulation of the elasto-plastic self-consistent polycrystal plasticity model and its implementation in implicit finite elements. Mech Mater 2019;136:103065.